

# The Development of CACTUS, a Wind and Marine Turbine Performance Simulation Code

Jonathan C. Murray\* and Matthew Barone†  
*Sandia National Laboratories, Albuquerque, NM, 87185*

**CACTUS (Code for Axial and Cross-flow Turbine Simulation) is a turbine performance simulation code, based on a free wake vortex method, under development at Sandia National Laboratories (SNL) as part of a Department of Energy program to study marine hydrokinetic (MHK) devices. The current effort builds upon work previously done at SNL in the area of vertical axis wind turbine simulation, and aims to add models to handle generic device geometry and physical models specific to the marine environment. An overview of the current state of the project and validation effort is provided.**

## Nomenclature

$b$	=	foil span
$c$	=	foil chord
$C_D$	=	drag coefficient
$C_L$	=	lift coefficient
$C_M$	=	moment coefficient
$U$	=	fluid velocity
$u$	=	x-axis velocity component
$v$	=	y-axis velocity component
$w$	=	z-axis velocity component
$X_T$	=	tip speed to freestream speed ratio
$\alpha$	=	angle of attack
$\dot{\alpha}$	=	angle of attack rate
$\Gamma$	=	circulation per length
$\sigma$	=	source strength per area

## I. Motivation

**I**N recent years, there has been a renewed interest in the use of vortex methods to study performance of both horizontal-axis and vertical-axis wind turbines at the engineering design level<sup>19,20,21</sup>. Although these methods have seen considerable use in similar analyses of fixed-wing aircraft and rotorcraft, engineering design of wind turbines has traditionally been carried out at a lower fidelity, using momentum methods to model the streamwise wake deficit and wake-induced flow. These methods may include detailed models of the response of the rotor to the local flow field that it experiences, but make simple algebraic approximations for the effect of the rotor loading on the rotor wake, and in turn, the wake on the local flow. The benefit of making such algebraic approximations is increased computational efficiency, but at the expense of any attempt to model the full time-dependent wake influence on the local flow at the rotor elements. Alternatively, dynamic inflow wake models<sup>22</sup>, borrowed from the rotorcraft industry and applied to horizontal axis wind turbines, approximate the time-dependent evolution of the rotor wake using solutions to the linearized, inviscid equations of motion. However, these models suffer from a lack of stability and accuracy for the full range of inflow and loading conditions experienced by a horizontal axis wind turbine, and do not include nonlinear effects such as vortex roll-up.

---

\* Aerosciences Department, Sandia National Laboratories/MS 0825, AIAA Senior Member.

† Wind and Water Power Technologies Department, Sandia National Laboratories/MS 1124, AIAA Senior Member.

Due to the increased computational cost in relation to momentum methods, codes based on vortex methods have historically seen most use in detailed analyses of final configurations. However, with advances in computing technology in recent decades, this area of work has come to be dominated by high-fidelity computational fluid dynamics (CFD) methods based on numerical solution of the Navier-Stokes equations. While these high-fidelity methods are very useful in this arena, there is benefit to developing vortex methods as a mid-fidelity option for system design, with more general capability than the momentum methods and at a fraction of the cost of full CFD. Vortex methods are quite general with respect to turbine geometry, and may be applied to both axial-flow and cross-flow turbines. They are especially good candidates for cross-flow turbine analysis, due to the complex nature of the wakes of these devices.

Sandia National Laboratories (SNL) has participated in the development of vortex methods for wind turbine analysis in the past. The VDART3 code, developed by Strickland at Texas Tech, under contract to SNL<sup>†</sup>, has seen wide use in the analysis of vertical axis wind turbines (VAWTs), specifically the Darrieus concept.

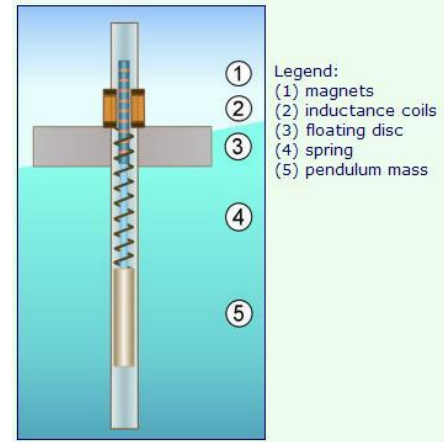
Beginning in 2009, the U.S. Department of Energy's Wind and Water Power Program initiated a research program to investigate and accelerate the technology development, deployment, and market acceptance of marine hydrokinetic (MHK) devices. The SNL portion of the program includes device performance prediction, advanced materials research, laboratory and field testing, site characterization, and environmental impact assessment, with the overall goal of promoting the reliable and affordable delivery of electricity from MHK devices.

MHK devices are generally grouped into three categories, referred to as wave, tidal, and in-river current. The present work deals with leveraging and expanding upon SNL's existing wind turbine analysis capabilities to provide analysis tools for MHK devices, primarily of the tidal or in-river current type (see Figure 1<sup>†</sup>). As such, work is ongoing to develop a vortex method code, CACTUS, for the simulation of turbine performance and wake structure, which will build on the existing VDART3 legacy by modernizing the solution approach and including models to handle generic device geometry and marine-specific physics. Ultimately, the goal of this work is to provide input to system level design in the areas of turbine performance and environmental impact assessment.

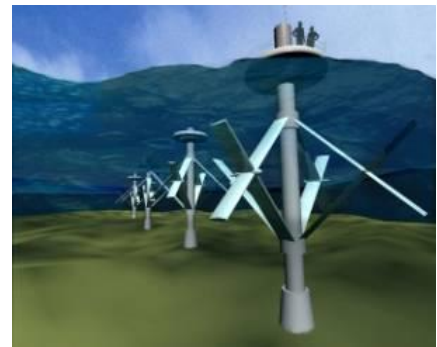
## II. General Capabilities

CACTUS simulates the fluid flow about, and blade loads on, a turbine device consisting of an arbitrary configuration of blade element sections in incompressible, largely inviscid, flow. Each blade element section has a span, a root and tip chord, and a root and tip twist value. Each section can be assigned arbitrary load coefficient vs. angle of attack characteristics, which typically correspond to two-dimensional lift and drag coefficient data for a particular foil section. Since data from two-dimensional wind tunnel tests or foil performance calculations are used to represent the entire section, it is generally assumed that these elements are in locally two-dimensional flow.

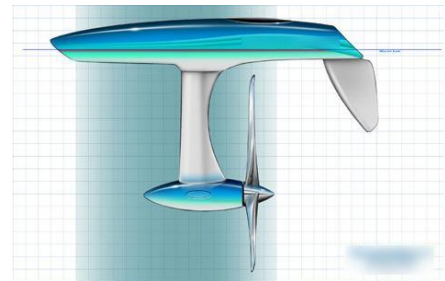
A rotor blade consisting of an arbitrary planform shape and foil sections can be modeled by the synthesis of a number of blade elements. The blade loads and wake of the turbine rotor are solved for in the time domain over a certain number of rotor revolutions, until the revolution-averaged rotor power is converged. The code output



a) Wave energy device



b) Tidal turbine device



c) In-river current device

**Figure 1. Types of MHK devices. Wave, tidal, and in-river current types shown<sup>†</sup>.**

<sup>†</sup> Source: U.S. Department of Energy Wind and Hydropower Technologies Program, *Marine Hydrokinetic Technology Database*, Accessed 12/04/10, <http://www1.eere.energy.gov/windandhydro/hydrokinetic/>

includes the blade aerodynamic forces, detailed wake vortex trajectories, and performance metrics such as torque and power.

In contrast to the simpler blade element momentum method, CACTUS uses an explicit, albeit reduced order, calculation of the fluid motion created by the blade elements to describe the local fluid flow conditions experienced by each individual element. At any time  $t$  during the simulation, the fluid flow field is represented as a linear superposition of potential flow elements: a freestream element, a vortex system composed of the trailing and spanwise wake vorticity, and a bound vortex system attached to the blade elements, as described in Figure 2. The bound vortex attached to each blade element is related to the lift coefficient for that element through application of the Kutta-Joukowski theorem<sup>2</sup>

$$\Gamma_B = \frac{1}{2} c U C_L \quad (1)$$

where  $C_L$  is the lift coefficient per unit span,  $c$  is the local chord length, and  $U$  is the local relative flow velocity magnitude. The wake created by the blade element system is represented by a time-dependent vortex lattice of trailing streamwise and spanwise vortex lines. The trailing and spanwise vorticity shed into the wake at each time step are equated to spanwise and temporal changes of the bound vorticity by the Helmholtz theorem of conservation of circulation along a vortex line<sup>2</sup>

$$\begin{aligned} \Gamma_T(y, t) &= \Gamma_B(y, t) - \Gamma_B(y - dy, t) \\ \Gamma_S(y, t) &= \Gamma_B(y, t - dt) - \Gamma_B(y, t) \end{aligned} \quad (2)$$

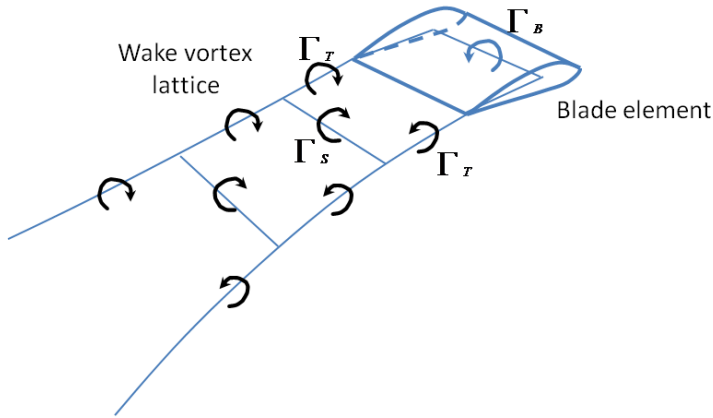


**Figure 2. Blade element with associated vortex lattice system.**

where  $y$  denotes the spanwise dimension and  $dy$  is the distance between blade element centers. The wake vorticity, once shed into an inviscid fluid flow, must translate and deform with the flow per Kelvin's theorem<sup>2</sup>, which states that the circulation around a closed contour moving with the flow is constant. Given a wake represented by a lattice of vortex line segments, this condition is satisfied if the lattice is evolved in time by advecting the lattice points with the local flow velocity.

The velocity field produced by any line segment element of the vortex lattice can be evaluated using the Biot-Savart law<sup>2</sup>

$$\mathbf{q} = \frac{\Gamma}{4\pi} \frac{\mathbf{r}_1 \times \mathbf{r}_2}{|\mathbf{r}_1 \times \mathbf{r}_2|^2} (\mathbf{r}_1 - \mathbf{r}_2) \cdot \left( \frac{\mathbf{r}_1}{|\mathbf{r}_1|} - \frac{\mathbf{r}_2}{|\mathbf{r}_2|} \right) \quad (3)$$

where  $\mathbf{q}$  is the resulting velocity vector at a point, with  $\mathbf{r}_1$  and  $\mathbf{r}_2$  being the vectors to that point from the ends of the vortex line segment.

Given a description of the wake vortex lattice system at any time  $t$ , the main thrust of the blade element formulation is to determine a set of blade element loads that are consistent with the local flow at each element produced by the current wake, freestream flow, and bound vorticity. The bound vorticity is used in calculating the local flow parameters used to determine the element load, and must also be related via Eq. (1) to the resulting element load. This implies a process in which an algebraic system is solved at each temporal iteration for the element loads and corresponding local flow velocity components due to the bound vorticity. This algebraic system can be represented as follows

$$\alpha_{element}, U_{element} = fn(\Gamma_B, \Gamma_T, \Gamma_S, freestream, geometry)$$

$$C_{L,element} = fn(\alpha_{element}, \dot{\alpha}_{element}, q_{element}, \dots)$$

$$\Gamma_B = fn(C_{L,element}, U_{element}, geometry) \quad (4)$$

Note that the relationship that determines the element lift coefficient may be non-linear due to non-linear static and dynamic foil section characteristics and/or modeling of dynamic stall effects. As such, CACTUS solves this algebraic system implicitly, using a simple fixed-point iteration. With a solution for the element loads and bound vorticity obtained, whole machine torque and power coefficients can be generated at time  $t$ , the wake system can be advanced to time  $t+dt$ , and the process can then repeat.

CACTUS currently uses a second-order predictor explicit time advancement scheme to advance the wake node positions in time. The scheme is based on the midpoint rule, with the state derivatives (wake node velocities) predicted at time  $t + \frac{\Delta t}{2}$  using the wake node velocities for the existing and previous time steps.

### A. Dynamic Blade Load Modeling

The aero- or hydrodynamic forces on a blade element consist of static aerodynamic coefficient data, augmented with dynamic derivatives to capture the first order effects of flow dynamics on element loads. These dynamic derivatives can be defined empirically, numerically, or by analogy to analytical solutions for simplified geometry (*e.g.*, a flat plate). They are meant to capture unsteady, attached-flow aerodynamic effects, including flow non-uniformity due to rotation, effects of induced flow due to spanwise wake circulation, and the added mass effect due to acceleration. Note that the wake modeling within CACTUS allows the effects of spanwise wake circulation to be represented explicitly.

Within CACTUS, the effects of foil rotation around the  $\frac{1}{2}$  chord location are accounted for by analogy with pitching flat plate theory<sup>2</sup>. An effective angle of attack,  $\alpha_{75}$ , calculated at the  $\frac{3}{4}$  chord location, is used to define the section lift coefficient. In this manner, the “circulatory” lift force, or lift due to instantaneous flow circulation around the foil, is modified to satisfy the Kutta condition in the presence of effective steady flow curvature due to rotation. The pitching flat plate theory also gives insight into so-called “added mass” effects on the foil force coefficients. These effects are due to additional flow accelerations on the foil surface, implied by a temporal rate of change of the flow circulation around the foil. The VDART3<sup>1</sup> code considered the added mass effects given by pitching flat plate theory to be a function of the pitch rate of the foil. This assumption resulted in an apparent cancellation between the added mass effect on the foil chordwise force and the component of circulatory lift in the foil chordwise direction.

In a departure from the original methodology used in VDART3<sup>1</sup>, the added mass effects on the foil force coefficients in CACTUS have been separated out and made a function of angle of attack rate,  $\dot{\alpha}$ , appropriately relating these effects to a temporally changing foil circulation. The resulting method for synthesizing the normal and chordwise (forward) force coefficients,  $C_N$  and  $C_T$  respectively, is given below. Note that  $\alpha_5$ , calculated at the  $\frac{1}{2}$  chord location, is used to define the section drag coefficient. This is done to maintain consistency with the axis system suggested by the pitching flat plate theory.

$$C_T = -C_{D,5}\cos(\alpha_5) + C_{L,75}\sin(\alpha_5) + C_{T,AM}(\hat{\alpha}_5)$$

$$C_N = C_{D,5}\sin(\alpha_5) + C_{L,75}\cos(\alpha_5)$$

$$C_{T,AM} = \frac{C_{L,5}}{2} \hat{\alpha}_5, \quad \hat{\alpha}_5 = \frac{\dot{\alpha}_5 c}{2U}$$

$$C_{L,75} = C_L(\alpha_{75}), \quad C_{L,5} = C_L(\alpha_5), \quad C_{D,5} = C_D(\alpha_5) \quad (5)$$

The operational cycle of some turbines, most notably cross-flow turbines, cause the turbine blades to operate at angles of attack beyond their steady-state stall limits for significant lengths of time. In addition, turbines operating at a typical tip speed ratio,  $X_T < 10$ , may see periods of stalled blade behavior due to freestream unsteadiness, large rotor yaw angles, and other transient operational conditions. The general effects of this transient stalled behavior on element aerodynamics are referred to as dynamic stall effects. Additional models for these dynamic stall effects are particularly necessary for an accurate description of turbine performance under these conditions<sup>3</sup>.

Two dynamic stall models are currently being studied within CACTUS.

### *Boeing-Vertol Empirical Correlation Model*<sup>6</sup>

This empirical correlation method keys on the phenomenological observation that a foil section appears to stall at a higher angle of attack,  $\alpha$ , when the stall condition is approached at a significant angle of attack rate,  $\dot{\alpha}$ . The modified Boeing-Vertol method of Gormont used here achieves this effect by modeling a “lagged”  $\alpha$  to be used in interpolating the user-provided steady-state lift, drag, and pitch moment coefficient data at points in the simulation where  $\alpha$  is outside of user-provided steady state stall limits. This lagged  $\alpha$  is reduced empirically as a function of the normalized  $\dot{\alpha}$  according to Eq. (6)<sup>1</sup>

$$\alpha_m = \alpha_b - K_1 \gamma \left( \left| \frac{c \dot{\alpha}}{2U} \right| \right)^{\frac{1}{2}} \quad (6)$$

where  $\alpha_m$  is the modified (lagged) angle of attack,  $\alpha_b$  is the geometric angle of attack, and  $K_1$  and  $\gamma$  are empirically defined constants. Note that the sign, and potentially the magnitude, of  $K_1$  varies with the sign of  $\dot{\alpha}$ . The method used here also defines a different lagged  $\alpha$ , using different  $\gamma$  values, for interpolating the lift, drag, and pitch moment coefficient data. Note that there are four empirical constants to be determined for any given foil to be modeled, in addition to the steady-state stall  $\alpha$  limits. This model has been used with reasonable success within VDART3<sup>1</sup>, where it has been shown that this model can give significant improvements in the modeled blade forces on a two-dimensional VAWT, provided the empirical constants are set appropriately. Unfortunately, the need to set the values of these constants to match existing data may limit the potential of this model as a predictive tool if the values prove to be overly sensitive to turbine or blade foil geometry.

### *Leishman-Beddoes Model*<sup>7,17</sup>

The Leishman-Beddoes model may provide a more fundamental means for synthesizing dynamic stall effects, which could improve the code’s ability to function as a predictive tool for design studies. The model synthesizes the effects of dynamic stall in the time domain as the solution of a set of first order differential equations in normalized time,  $s = t * (2U/c)$ , with the value in parentheses being the inverse of a time scale based on foil chord and relative fluid velocity. These differential equations model the dynamics and interactions of three primary phenomena that govern the blade loads during dynamic stall, discussed below.

**Phases of Leading Edge Separation:** The Leishman-Beddoes model generally describes the dynamic stall process in terms of phases; leading edge vortex build-up, leading edge vortex shedding, full stall, and reattachment. The onset of leading edge vortex shedding is assumed to occur when the leading edge pressure gradient reaches some critical value. The model considers this critical pressure gradient to be achieved when the ideal (linear) lift coefficient exceeds a critical lift coefficient value,  $C_{L,crit}$ . For a particular foil, the critical lift coefficient can generally be equated to the value of the ideal lift coefficient that would exist at the observed maximum lift coefficient angle of attack, had the lift coefficient remained linear with angle of attack. On a foil undergoing a dynamic pitching motion, the realization of this critical leading edge pressure gradient is observed to be delayed to higher angles of attack than observed in the steady state<sup>7</sup>. This delay can be represented by lagging the ideal lift coefficient to be compared with the critical value. A first order lag ordinary differential equation with a time constant defined in normalized time,  $T_p$ , is used for this purpose.

Following the onset of leading edge vortex shedding, the model enters the second phase in which the leading edge vortex is considered to move across the chord over a normalized time period,  $T_{vl}$ . As the normalized time from the onset of vortex shedding exceeds twice  $T_{vl}$ , and provided the ideal lift coefficient is still in excess of  $C_{L,crit}$ , the model enters the full stall phase. Once the ideal lift coefficient has dropped below  $C_{L,crit}$ , the model enters the reattachment phase, in which the model behaves as it did prior to the onset of leading edge separation.

**Trailing Edge Separation:** An approximation of the trailing edge separation point location is used to reference the forces acting on the foil throughout all phases of the model. This is achieved using the theory of Kirchhoff, following an approach similar to the one described in the original formulation of the model<sup>7</sup>. The approach has been modified to operate on arbitrary static section force coefficients in a manner similar to that proposed in Ref. (10). The resulting representation of the lift coefficient is

$$C_{L,f} = C_{L,sep}(\alpha) + \frac{1}{4} C_{L,ID}(\alpha) [f + 2\sqrt{f}] \quad (7)$$

where  $f$  is in the range  $[0,1]$  and generally denotes the position of the trailing edge separation point with  $f = 1$  at the trailing edge, and  $f = 0$  at the leading edge. The values  $C_{L,ID}$  and  $C_{L,sep}$  are the full attached and fully separated values of the lift coefficient. The fully separated value is nominally set as  $C_{L,sep} = \frac{1}{4} C_{L,ID}$ ; however, this setting may be overridden to match the static section coefficient data at large values of angle of attack. The fully attached value is nominally defined as the ideal (linear) lift coefficient value, although for practical purposes, this value is limited at large values of angle of attack. Details of this limiting are given in Ref. (10).

By matching Eq. (7) to the static section force coefficients for a given foil, one could define an effective trailing edge separation point position for the static foil,  $f_{stat}$ . On a foil undergoing dynamic pitching motion, the trailing edge separation point is seen to lag the static value, causing a delay in the appearance of separated flow effects. The Leishman-Beddoes model treats this as a first order lag with a time constant,  $T_f$ . This time constant may be varied depending on the phase of the leading edge separation model.

**Vortex Lift:** The Leishman-Beddoes model includes an effect of vortex lift attributed to the dynamic shedding of vorticity from the leading edge, and the subsequent motion of these shed vortices across the chord of the foil. This effect is most prevalent during the leading edge vortex shedding phase of the model. The shed vortex effect is applied as a force normal to the foil, and is modeled as an increment to the foil circulation that decays over a time period,  $T_v$ . The initial increment to circulation due to a shed vortex is attached to the rate change of circulation bound to the foil due to upper surface flow separation. A first order lag differential equation is employed to model the decay of the vortex lift effect, which is expressed in terms of an increment to the normal force coefficient,  $C_{N,v}$ . The resulting ordinary differential equation is given below. To avoid potentially generating non-physical effects of negative leading edge vortex shedding<sup>10</sup>, the vortex feed term,  $F_v$ , has been limited to only “positive” shedding values, that is,  $F_v$  is set to zero if its sign is opposite  $C_{L,ID}$ .

$$\frac{dC_{N,v}}{ds} = \frac{F_v - C_{N,v}}{T_v}$$

$$F_v = \frac{d}{ds} (C_{L,ID} - C_{L,f}) \quad (8)$$

Currently, in CACTUS, the states defined in the Leishman-Beddoes model as solutions to first order lag differential equations are advanced in time using the Duhamel decomposition solution technique<sup>17</sup>, with an explicit mid-point integration rule. The deficiency in each state from its steady-state value can then be updated through each normalized time step with a discrete recursion relation of the form

$$D_{s+ds} = D_s e^{\frac{-ds}{T}} + F e^{\frac{-ds}{2T}} \quad (9)$$

where the feed term,  $F$ , is the change in the steady-state value over the normalized time step,  $ds$ , and  $T$  is the first order lag time constant.

Many practical considerations for robust application of the Leishman-Beddoes model to the wind or MHK turbine problem are handled within CACTUS in a manner similar to that discussed in Ref. (10). As the dynamic load cycle progresses through the phases described above, changes in the relevant physical processes are represented within the model by changing the time constants associated with the motion of the trailing edge separation point and the vortex lift response. This is accomplished in a manner similar to that discussed in Refs. (8, 9). It is suggested<sup>7</sup> that these time constants, set for each logical phase of the model, should be fairly independent of the foil shape. An effort to verify these time constants for hydrofoil shapes of relevance to MHK turbine blades is underway.

## B. Turbine Geometry

There is great variety in proposed and prototype MHK turbine systems, including many variations on both axial and cross-flow rotors. An effort has been made to generalize the treatment of problem geometry used within CACTUS, decoupling the specifics of the geometry from the solution method. This allows the code to simulate different configurations of rotor and boundary geometry while using the same calculation engine. An arbitrary turbine configuration can be constructed by generating blade structures discretized with a set of potential flow elements, and specifying a rotation axis and a rotation rate. Boundary geometry can be discretized with a set of potential flow source panel elements with either symmetry or free-surface boundary conditions applied.

At present, geometry creation is performed with a geometry module integral to CACTUS, with the user specifying basic design parameters specific to axial or cross-flow type geometries. This function is planned to be removed to an external geometry specification process, possibly implemented in MATLAB, with the goal of allowing the user to specify more general geometry without the need to modify the CACTUS source code.

CACTUS geometry objects are described below:

#### *Lifting Line Blade*

Currently, the geometry creation module allows the user to specify generic axial and cross-flow type turbine geometries using basic design parameters as inputs. The basic specification used to generate each geometry type is described in Figure 3. CACTUS currently represents the cross-flow type blade shape with either a parabolic shape function described by Eq. (10), or a straight-bladed shape with  $r/R = 1$ . These rotor geometries are defined given an input height to maximum radius ratio,  $H/R$ . Both axial and cross-flow type geometries can make use of a variable chord and foil section specification along the length of the blade. Axial rotor blades can also have a pitch angle with respect to the rotor disk plane, as well as a variable twist along the length of the blade.

$$\eta = 1 - 4 \left( \frac{\zeta}{H/R} \right)^2, \quad \eta = \frac{r(s)}{R}, \quad \zeta = \frac{y(s)}{R} \quad (10)$$

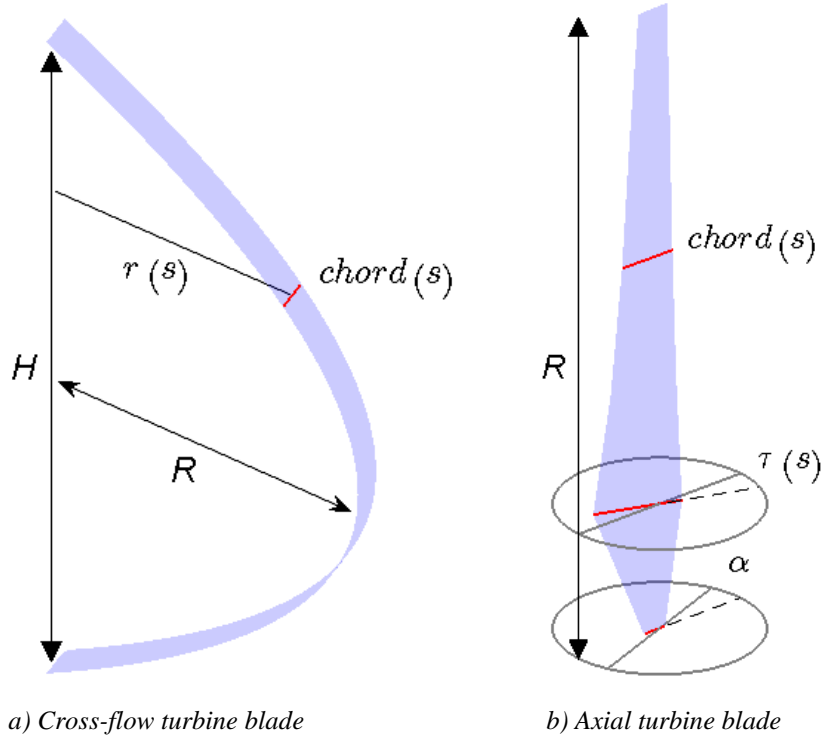


**Figure 3. Blade geometry for cross-flow and axial turbine blades**

#### *Strut and Blade/Strut Interference Drag*

Many cross-flow turbine designs feature support struts that either connect the rotor blades to the rotating shaft or otherwise stiffen the rotor structure. It is essential to account for the drag introduced by the strut when calculating rotor torque and power. There are two primary components of strut drag: the profile drag of the strut member itself, and the interference drag at the strut/blade attachment point. In CACTUS, support struts are divided into a number of elements, and a decrement in torque is calculated for each element at each time step. For a given strut sectional thickness, the element drag is determined from semi-empirical relations for the profile drag coefficient of foil sections as a function of local chord Reynolds number given in Hoerner<sup>16</sup>. The local angle of attack seen by a strut element is assumed to remain small, such that the profile drag is a good approximation of the total drag experienced by the element. The profile drag coefficient, along with the local flow velocity relative to the strut (including free-stream and wake-induced components) is then used to compute the torque decrement. The interference drag

experienced at the strut/blade attachment point is calculated using the following empirical relation for drag coefficient of the junction of two foil sections intersecting at ninety degrees<sup>16</sup>:

$$C_{dj} = \left(\frac{t}{c}\right)^2 17.0 \left(\frac{t}{c}\right)^2 - 0.05 \quad (11)$$

Here,  $\frac{t}{c}$  is the average thickness-to-chord ratio of the two foils. The reference area for this junction drag coefficient is the square of the chord at the foil intersection.

### C. Boundary Conditions for MHK Turbine Problems

MHK turbines may be deployed near river or tidal beds, or close to the water surface. The flow restrictions due to such boundaries can impact turbine performance. CACTUS is capable of simulating these effects using solid surface or fluid free surface boundary planes. These boundary conditions are enforced using constant-strength source panel elements in a manner similar to many first-order linear potential flow computational fluid dynamics methods. As no net circulation is to be produced on these boundary elements, source panel elements are an efficient choice.

#### *Solid Surface Boundaries*

At present, CACTUS synthesizes wall boundary conditions using rectangular constant-strength source panels. Relations for the velocity and potential fields generated by a variety of individual panel singularity elements can be found in Katz and Plotkin<sup>2</sup>. The rectangular, constant-strength source panel used in CACTUS can be reduced from the relations for an arbitrary quadrilateral panel. The velocity field produced by this panel singularity, relative to panel coordinates, is given in Eqs. (12-17). In the limit that the evaluation point reaches the surface of the panel, the panel normal velocity is directly related to the panel source density, and the panel tangential velocities vanish. This makes the source panel attractive for synthesizing and solving the large linear solution matrices that will enforce the desired boundary conditions.

$$u = \frac{\sigma}{4\pi} \left[ \ln \left( \frac{(|r_1|+|r_2|-W)(|r_3|+|r_4|+W)}{(|r_1|+|r_2|+W)(|r_3|+|r_4|-W)} \right) \right] \quad (12)$$

$$v = \frac{\sigma}{4\pi} \left[ \ln \left( \frac{(|r_4|+|r_1|-L)(|r_2|+|r_3|+L)}{(|r_4|+|r_1|+L)(|r_2|+|r_3|-L)} \right) \right] \quad (13)$$

$$w = \frac{\sigma}{4\pi} \left[ \tan^{-1} \left( \frac{h_1}{r_{c,z}|r_1|} \right) + \tan^{-1} \left( \frac{h_3}{r_{c,z}|r_3|} \right) - \tan^{-1} \left( \frac{h_2}{r_{c,z}|r_2|} \right) - \tan^{-1} \left( \frac{h_4}{r_{c,z}|r_4|} \right) \right] \quad \text{where, } h_i = r_{i,x}r_{i,y} \quad (14)$$

$$\frac{\partial u}{\partial x} = \frac{\sigma W}{2\pi} \left[ \frac{\frac{r_{1,x}}{|r_1|} + \frac{r_{2,x}}{|r_2|}}{(|r_1|+|r_2|+W)(|r_1|+|r_2|-W)} - \frac{\frac{r_{3,x}}{|r_3|} + \frac{r_{4,x}}{|r_4|}}{(|r_3|+|r_4|+W)(|r_3|+|r_4|-W)} \right] \quad (15)$$

$$w(z = 0^+) = \frac{\sigma}{2} \quad (16)$$

$$\frac{\partial u}{\partial x}(\text{center of panel, } z = 0^+) = \frac{2\sigma}{\pi L} \sqrt{\frac{1}{1 + \left(\frac{L}{W}\right)^2}} \quad (17)$$

$L$  and  $W$  are the panel extents in the panel-x and panel-y directions,  $r_1$  through  $r_4$  are vectors to the point of interest from the corners of the panel, ordered clockwise, viewed from the positive panel-z side, from the minimum x and y corner, and  $r_c$  is the same but from the center of the panel. Note that the inverse tangent here is the 2-quadrant version with limits  $[-\pi/2, \pi/2]$ .

To verify the correctness of the rectangular panel approach to applying wall boundary conditions, a simple two and three dimensional symmetry plane study was performed with the symmetry plane enforced using rectangular panels, and using exact (in infinite series) method of images solutions as truth source data<sup>2</sup>. The symmetry plane, or solid wall, boundary condition is zero normal flow:

$$\nabla \Phi \cdot \hat{n} = 0 \quad (18)$$



where  $\Phi$  is the velocity potential, and  $n$  is the panel normal unit vector.

The geometry for the test computation consists of a point singularity disturbance centered in a channel formed by two planes of source panels oriented parallel to a freestream in the  $x$  direction. The point singularity is separated from the two walls by a distance,  $D$ , in the  $z$  direction. Both source and doublet point singularities were used, mainly

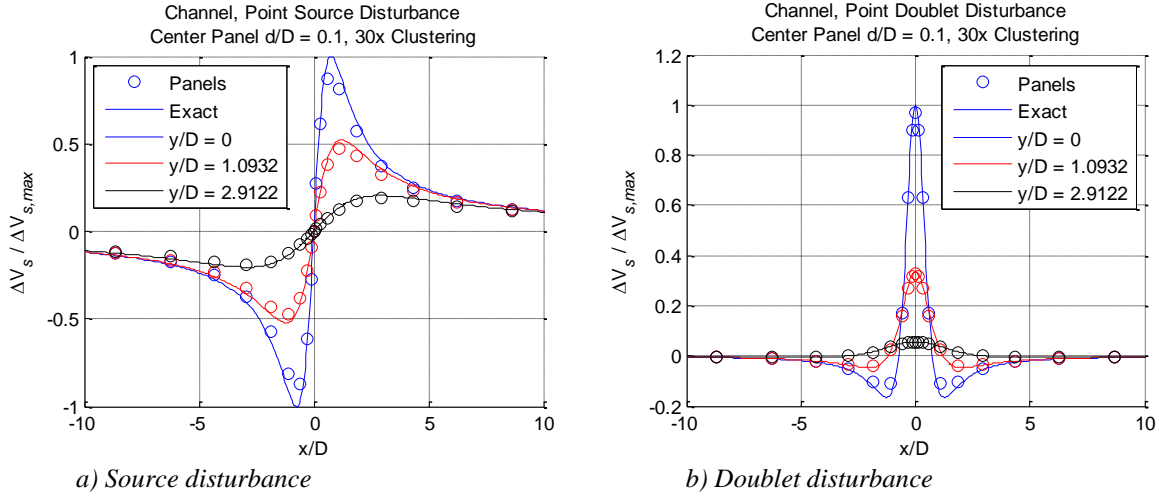


**Figure 4. Velocity perturbation on channel surface represented with rectangular source panels due to point disturbances.**

for the purpose of evaluating the wall panel system extents required to adequately capture the particular effects of wake-like blockage (point source) and streamlined blockage (point doublet). Results of this study are shown in Figure 4 in terms of the velocity perturbation from freestream in the  $x$  direction along the channel walls. The velocity perturbation is normalized by the maximum value of the perturbation in the exact solution. Three lateral stations are represented, with the point singularity located at  $x/D = 0$  and  $y/D = 0$ . The wall system extends  $-10 < x/D < 10$  and  $-10 < y/D < 10$  using a total of 360 panels on each wall, clustered 30 times more dense in the center, near the point singularity. Errors of approximately 1-5% on surface velocity are seen at the center of the system with this level of discretization.

#### Free Surface Boundaries

Using the same rectangular panel method, the effects of a steady fluid free surface boundary condition can be simulated. The term “free surface” refers to the fact that the fluid surface is free to move and, in the presence of a disturbance, will adjust to seek an equilibrium condition. Neglecting surface tension forces, that equilibrium condition is characterized by a constant pressure across the surface. Note that in order for this boundary condition to be valid, the influence of gravitational forces on the fluid flow must be significant, that is, the Froude number

$Fn = \sqrt{\frac{U^2}{gL}} \leq 1$ , where  $U$  is the characteristic flow velocity,  $L$  is the characteristic length scale, and  $g$  is the gravitational acceleration. Note that the choice of characteristic length scale for the free surface response is specific to the geometry of the problem under consideration. An MHK turbine submerged beneath a free surface will present two possible length scales, the turbine geometry scale,  $R$ , and the submergence depth,  $D$ . In the limit,  $\frac{D}{R} \gg 1$ , one can expect the free surface response in the vicinity of the turbine to scale with depth, whereas in the opposite limit, one can expect the response to scale with turbine size. Some proposed MHK turbine configurations will operate with  $\frac{D}{R} \approx O(1)$ , indicating that both length scales may affect the character of the free surface response. Froude numbers based on either of these length scales will be on the order of 1 for many of the MHK turbine configurations we plan to study.

For a free surface nominally oriented normal to the gravitational acceleration vector, the linearized free surface boundary condition<sup>4</sup> is

$$U_\infty^2 \frac{\partial^2 \phi}{\partial x^2} + g \frac{\partial \phi}{\partial z} = 0 \quad (19)$$

where the freestream velocity is oriented in the x direction with magnitude  $U_\infty$ , and the gravitational vector is oriented in the z direction with magnitude  $g$ . This condition, derived from the steady Bernoulli relation keeping the gravitational potential term (low  $Fr$ ), physically represents a balance between the pressure gradient effects of flow acceleration along the surface, and gravitational potential change along the surface due to surface inclination.

One common approach to applying Eq. (19) is to satisfy the boundary condition at the location of the undisturbed free surface<sup>2</sup>. With this simplification, the potential gradient in the second term in Eq. (19) becomes the velocity normal to this undisturbed free surface. The first term is related to changes in velocity in the direction of the nominal freestream. This condition can be enforced using the rectangular source panel method discussed previously. Note that, in contrast to the solid wall, the dividing stream-surface produced by the source panel system using the free surface boundary condition, which defines the extent of the physically relevant domain of the calculation, may be displaced from the surface on which the source panels reside. To avoid non-physical solution behavior, it is typical to place the source panel system outside the solution domain, displaced from the undisturbed free surface (where the boundary condition is to be satisfied) by a distance larger than the maximum expected free surface deviation from its undisturbed state<sup>2</sup>.

In addition to specifying the free surface boundary condition on the surface panels, an inflow boundary condition is required to force the flow (far) upstream of any disturbance to remain at freestream conditions. Physically, this is referred to as a radiation condition, and is needed to reject the natural response of Eq. (19) to waves of infinite extent, described later in this section. This is done on the grounds that standing waves, steady in the frame of the disturbance, cannot have propagated upstream of the disturbance.

There are a variety of ways to effect the necessary inflow boundary condition. One commonly used implicit approach is to simply shift the collocation points for the surface panels upstream by a distance on the order of the paneling scale. This, in effect, forces the free surface boundary condition to be satisfied such that the solution has attenuated response at the upstream extent of the grid, due to the fact that the upstream collocation points are “hanging” out in the nominal freestream.

An alternative, less heuristic, method is to apply an explicit inflow boundary condition, without shifting collocation points, by forcing the derivative of the velocity along the surface to zero on the upstream extent of the grid. In order to enforce both the free surface boundary condition and the inflow condition on the upstream row of collocation points, an additional row of “hanging” panels are added to keep the linear system balanced. As the free surface boundary condition is not explicitly satisfied on these panels, it is unadvisable to add this row of hanging panels at the upstream extent of the grid. If this is done, the inflow boundary condition is seen to be satisfied primarily by grid scale solution modes, with the effects localized around the upstream extent of the grid. This solution is non-physical in the sense that, while it solves the discretized set of equations, the solution variations near the grid scale corrupt the intended physical boundary condition. If instead, the hanging panel row is added at the downstream extent of the grid (with the inflow conditions remaining on the upstream collocation points), both the free surface boundary condition and inflow condition are seen to be satisfied as intended, in a physically relevant manner. This method of applying the inflow boundary condition is employed in CACTUS.

#### *Verification of the Free Surface Boundary Condition*

Analytical solutions exist for planar surface waves of infinite extent, derived from complex potential theory used to satisfy the linearized boundary condition, Eq. (19), on the free surface boundary<sup>4</sup>. The linear plane wave system described by this solution is dispersive, that is, the frequency of a plane wave component is a function of its wavelength, as given below.

$$\omega^2 = gk * \tanh(kd), \quad k = \frac{2\pi}{\lambda} \quad (20)$$

where  $\lambda$  is the wavelength,  $\omega$  is the frequency, and  $d$  is the water depth. Note that in the shallow water limit,  $\frac{\lambda}{d} \gg 1$ , the dispersive behavior of the wave system disappears, with the wave phase velocity,  $U_p = \frac{2\pi\lambda}{\omega} = \sqrt{gd}$ , becoming independent of wavelength. This non-dispersive shallow water solution is directly analogous to linear compressible aerodynamics. Here, the Froude number based on water depth is equivalent to the Mach number: a ratio of characteristic fluid speed to the gravitational wave speed in the case of the Froude number and the acoustic wave speed in the case of the Mach number.

The above analogy isn't quite as direct in the deep-water limit due to the effects of superimposing dispersive waves. Using the plane wave phase speed, the deep water limit of the dispersion relation in Eq. (20) can be rewritten as

$$2\pi Fn_\lambda^2 = 1 \quad (21)$$

where  $Fn_\lambda$  is a Froude number based on the phase speed and wavelength of the plane wave.

Considering a disturbance of characteristic scale  $L$ , in a freestream flow moving at a speed,  $U_\infty$ , steady waveforms in the frame of the disturbance propagating at an angle  $\theta$  from the freestream velocity must have phase velocity,  $U_p = U \cos(\theta)$ . This implies a relation between the wavelength of a plane wave and the angle at which it propagates, which, making use of Eq. (21), is given below.

$$\frac{\lambda}{L} = 2\pi \cos^2(\theta) Fn_L^2 \quad (22)$$

where  $Fn_L$  is a Froude number based on  $U_\infty$  and  $L$ .

Using a technique referred to as the method of stationary phase, the far-field wave train trailing a disturbance resulting from a superposition of dispersive plane waves described by Eq. (22) can be described by two dominant modes<sup>5</sup>. Shape functions for the transverse and diverging wave modes are given below.

$$\begin{aligned} \theta_T &= \frac{\alpha}{2} - \frac{1}{2} \sin^{-1}(3 \sin(\alpha)) \\ \theta_D &= -\frac{\pi}{2} + \frac{\alpha}{2} + \frac{1}{2} \sin^{-1}(3 \sin(\alpha)) \\ |\alpha| &< 19.47^\circ \end{aligned} \quad (23)$$

where  $\theta$  is the angle of the propagating wave front and  $\alpha$  is the polar angle around the disturbance from the direction opposite the disturbance velocity. Note that angles of propagation up to 35.16 degrees are found on the transverse mode, whereas angles from 35.16 to 90 degrees are found on the diverging mode. This wave system is referred to as the Kelvin wave train, and the angle of the envelope in which it fits,  $K \cong 19.47^\circ$ , is called the Kelvin angle. It should be noted that the term “far-field” used above generally refers to downstream distances,  $\frac{x}{L} \gg 1$ .

Although an approximate concept, it can be useful to define a dominant angle of propagation using Eq. (22), and generally equating the dominant wavelength in the wave train to the characteristic disturbance length scale,  $L$ . This produces a relation similar to the Mach angle relation in linear compressible aerodynamics, shown below.

$$\theta_L = \cos^{-1} \left( \frac{1}{\sqrt{2\pi} Fn_L} \right) \quad (24)$$

Note the difference from linear compressible aerodynamics: in the deep water limit, the envelope of the wake is

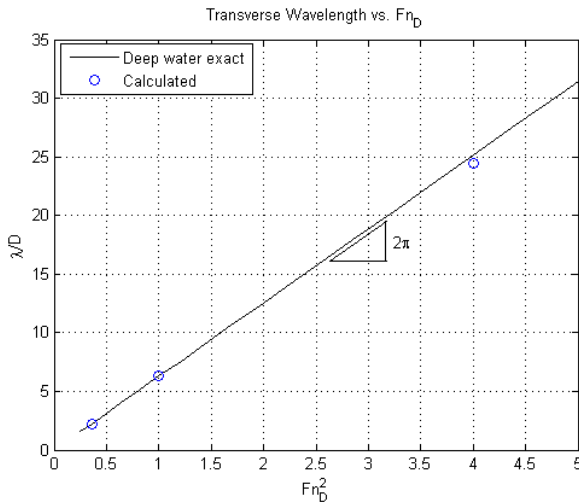


**Figure 5. Transverse wavelength extracted from rectangular panel simulations.**

not dependant on Froude number, in contrast to the way the Mach number would affect the Mach angle. The Froude number will, however, affect the scale of the transverse and diverging wave modes, and the dominant angle of propagation, found within the Kelvin envelope.

Simulations of a point disturbance submerged at a depth,  $D$ , under a free surface have been performed, with the free surface boundary condition enforced using rectangular source panels and an inflow boundary condition applied as discussed above. The disturbance is simulated with a simple point doublet oriented along the freestream flow axis. As such, the free surface response simulated here is representative of the limit in which the depth is large with respect to the turbine size. Consequently, the Froude number based on submergence depth,  $Fn_D$ , is used to

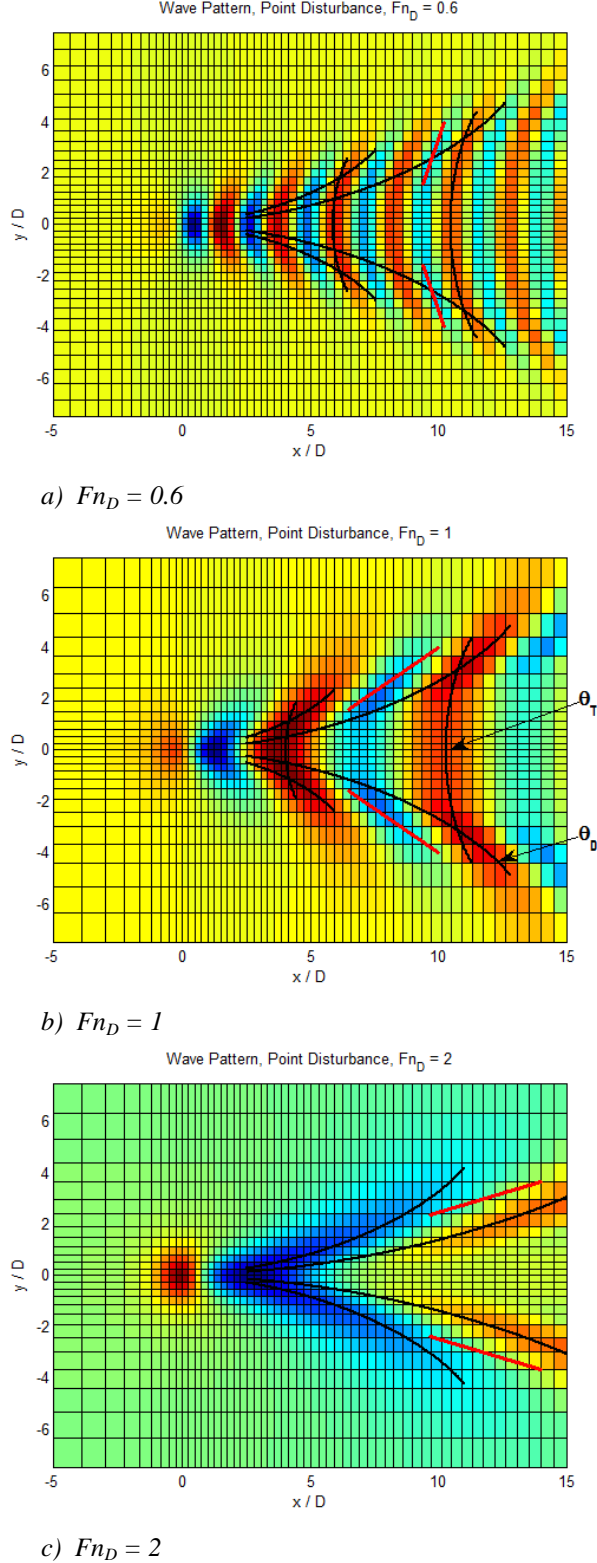


**Figure 6. Wave patterns behind a point disturbance.** Rectangular source panels with inflow boundary conditions on the upstream grid boundary (left on plot). Colors represent wave height (+ red).

describe the free surface response.

Simulation results are compared with the far-field wake descriptions given by the method of stationary phase in Figure 6. The black lines on the plots represent the transverse and diverging wave modes with shapes given by Eq. (23), and the red lines represent the dominant angle of propagation given by Eq. (24). The dominant angle of propagation is defined here with the assumption that the characteristic disturbance length scale is approximately twice the submergence depth. The scaling of the wavelength of the transverse waves with Froude number, observed along the x-axis in Figure 6, is shown in Figure 5 to be in good agreement with the expected deep water scaling given by Eq. (22).

Grid scale requirements for the free surface panel grid need to be considered to avoid a poorly conditioned solution. The near field free surface response scales with characteristic disturbance scale,  $L$ , which may be related to the submergence depth or the turbine scale. The grid scale downstream of the disturbance generally needs to be kept at this level to allow wavelengths of this scale to propagate into the wake. Note, however, that if the Froude number is allowed to decrease indefinitely, the solution will become dominated by transverse waves of indefinitely decreasing scale. This will eventually destabilize the calculation performed on a grid sized for the near field solution, once the scale of the wave train defined by Eq. (22) descends below the near field scale. Physically, however, this situation represents the free surface boundary condition approaching its low Froude number limit. In this limit, the free surface boundary becomes equivalent to the solid wall boundary (zero normal flow), and the solution limits to that found by replacing the free surface with a solid wall. As such, the current simulation deactivates the free surface boundary condition in favor of the solid wall boundary condition at Froude numbers where the transverse wave scale, defined by Eq. (22), cannot be accurately represented by the user-specified grid resolution for the near field.

The treatment of the free surface boundary condition described above assumes a steady solution in the frame of the object creating the disturbance. As the temporal dynamics of the free surface are not currently represented, CACTUS implements the free surface boundary condition as a quasi-static boundary, allowing it to respond only to the average flow created by the turbine and wake over a full revolution.

### III. Validation

The ability of CACTUS to accurately predict the power of cross-flow turbines is assessed by comparing simulation results with measured data for Vertical-Axis Wind Turbines (VAWTs). Note that the rigid-body aerodynamics of a wind turbine and the hydrodynamics of a MHK turbine (neglecting boundary effects) are essentially the same in terms of flow physics, the exception being the possibility of cavitating flow in water.

Operational turbines often exhibit a lower level of performance than would be expected from the analysis of sub-scale test articles, or preliminary design calculations. This is most often due to increased aerodynamic drag due to a multitude of relatively small excrescences from the designed ideal aerodynamic shape that are unavoidable on practical machines. Fasteners, joints, or support mechanisms in place on the operational devices all contribute to this excess drag. With a detailed description of the “as built” geometry of an operational turbine, one can make a fairly accurate prediction of the total excrescence drag to be expected on an operational device using simple superposition of effects. The individual drag characteristics of various types of excrescences can be found in handbooks such as Ref. (16). Lacking this detailed geometry information, an estimate of the excrescence drag can be obtained from a comparison of predicted drag with experimental data taken with the turbine rotor revolving in zero wind conditions. CACTUS can apply a user specified machine-level excrescence torque coefficient defined as

$$C_{T,Ex} = \frac{\Delta Torque}{\frac{1}{2}\rho U_{tip}^2 R^3} \quad (25)$$

where  $\Delta Torque$  is the added torque due to excrescences,  $\rho$  is the fluid density,  $U_{tip}$  is the rotor blade tip speed, and  $R$  is the rotor radius. For the purpose of building up the cumulative effect of known excrescences from a detailed geometry description, the machine-level excrescence torque as defined above can be related to the drag of individual excrescences as

$$C_{T,Ex} = \sum_i C_{D,Ex_i} \left( \frac{A_{Ex_i}}{R^2} \right) \left( \frac{R_{Ex_i}}{R} \right)^2 \quad (26)$$

where the subscript,  $i$ , refers to the individual excrescence, and  $A_{Ex}$  and  $R_{Ex}$  are the drag coefficient reference area and radial location of the excrescence.

#### D. Sandia 5m VAWT

The Sandia 5 meter-diameter<sup>§</sup> VAWT research turbine<sup>12</sup> is shown in Figure 7. The rotor for this turbine consisted of either two or three curved blades rotating about a central tower. The rotor height-to-radius ratio was 2.04. The extruded aluminum blades were bent to a composite straight line/circular arc shape. The airfoil section was a NACA-0015 along the entire length of the blade. The blades were of constant chord equal to 6 inches, giving a rotor solidity of 0.15 for the two-blade configuration and 0.22 for the three-blade configuration. Performance data were collected and averaged in order to obtain a mean performance curve, representing statistically averaged power coefficient versus mean wind speed at the rotor equator height. The power coefficient data were corrected for drive train losses, resulting in a reported aerodynamic rotor power coefficient, facilitating direct comparison to CACTUS results.

CACTUS simulations were run for three cases where data were collected: the two-bladed configuration with a rotational speed of 162.5 RPM, and the three-bladed configuration at 125 and 150 RPM. The airfoil performance data for the NACA-0015 were taken from Ref. (13). Excrescence drag was accounted for using the zero-wind speed profile blade drag coefficient reported from the experiment. The measured profile drag coefficient was about 20%

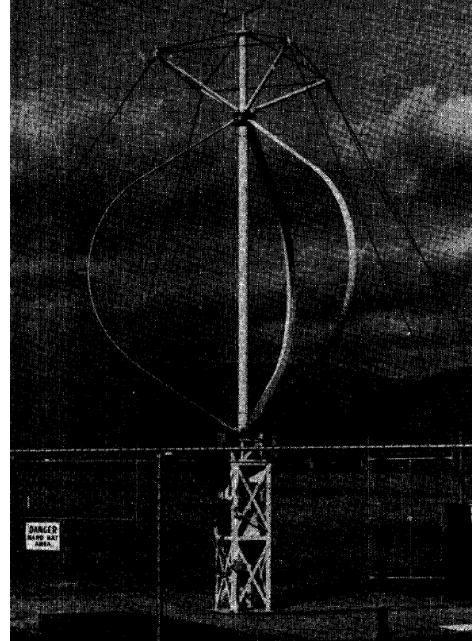


Figure 7. The Sandia 5 meter VAWT

<sup>§</sup> The actual diameter of this “5-meter” rotor was 15 feet, or 4.57 meters.

higher than the profile drag of the airfoil performance data in the relevant Reynolds number range. The simulations were run with a constant mean wind speed; the effect of wind shear on the results should be explored in further validation studies. For tip speed ratios less than six, the simulations were run for 15 rotor revolutions or until the power coefficient converged to less than 0.1%. For higher tip speed ratios the simulations were run for 20 revolutions. The reported power coefficient is the average value over the final simulated revolution. The blades were each discretized with 13 vortex elements, and each revolution was resolved by twenty time steps. The modified Boeing-Vertol dynamic stall model was used in these simulations. Results are presented as power coefficient versus tip speed ratio. Power coefficient is defined in Eq. (27), where  $U$  is the mean wind speed,  $\rho$  is the air density, and  $A$  is the rotor swept area. Tip speed ratio is defined in Eq. (28), where  $\Omega$  is the rotational speed and  $R$  is the rotor equatorial radius.

Figure 8 shows the predictions for the two-bladed configuration. Power is well-predicted at low and high tip-speed ratios, while peak power coefficient is over-predicted by approximately 10%. Improved agreement is demonstrated in Figure 9 for the three-bladed configuration at 125 RPM. The results for the three-bladed rotor at 150 RPM are shown in Figure 10. The measured data show a significant increase in peak  $C_p$  over the 125 RPM case, compared with a very modest predicted increase. This results in a slight under-prediction of the peak  $C_p$ . Due to its small size, this turbine operated at relatively low chord Reynolds numbers:  $2.5 \times 10^5$  at 125 RPM and  $3 \times 10^5$  at 150 RPM. Evidently the turbine performance was very sensitive to small changes in Reynolds number, and this effect is not fully captured by the CACTUS model. Nevertheless, these results demonstrate a sufficient level of accuracy for CACTUS to be useful as a cross-flow turbine design code.

$$C_p = \frac{P}{\frac{1}{2}\rho U^3 A} \quad (27)$$

$$X_T = \frac{\Omega R}{U} \quad (28)$$

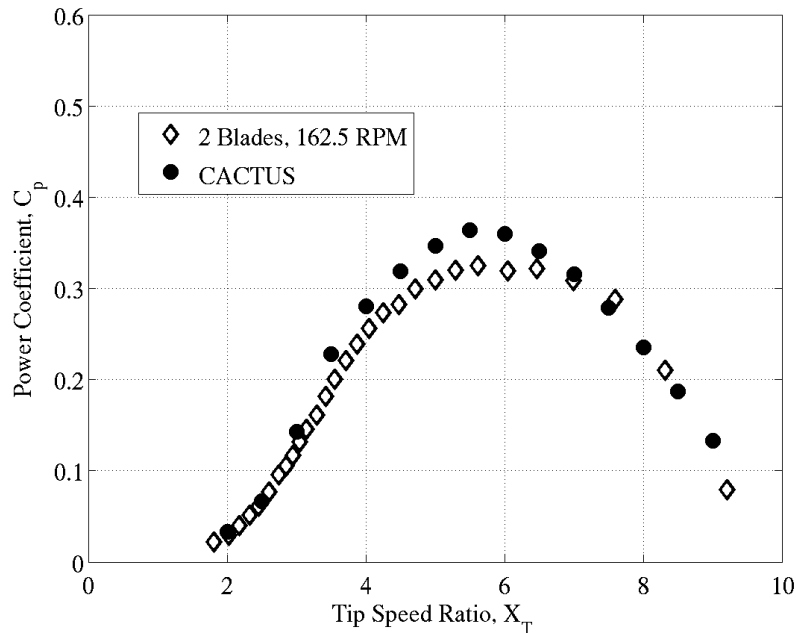


**Figure 8. CACTUS power coefficient prediction with Sandia 5 meter VAWT measured data; 2 blades, 162.5 RPM.**

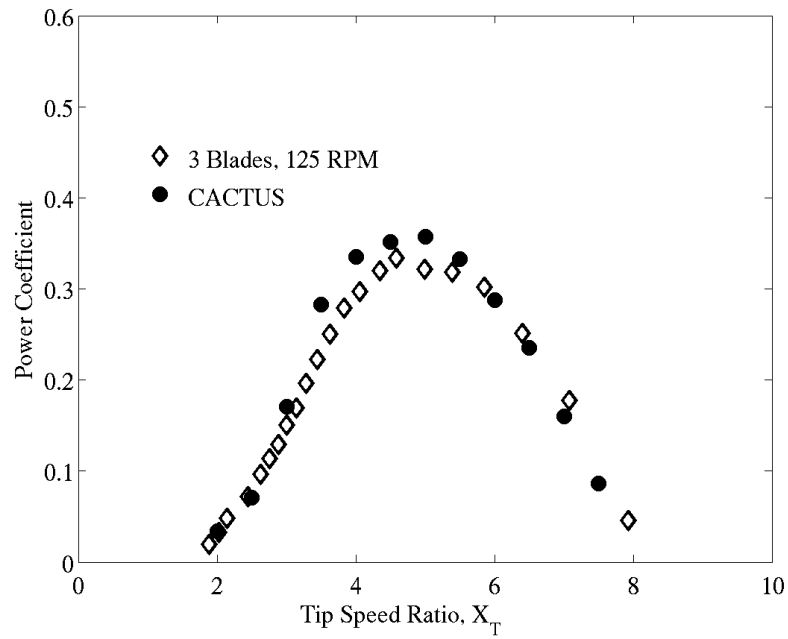


**Figure 9. Comparison of CACTUS power coefficient prediction with Sandia 5 meter VAWT measured data; 3 blades, 125 RPM.**

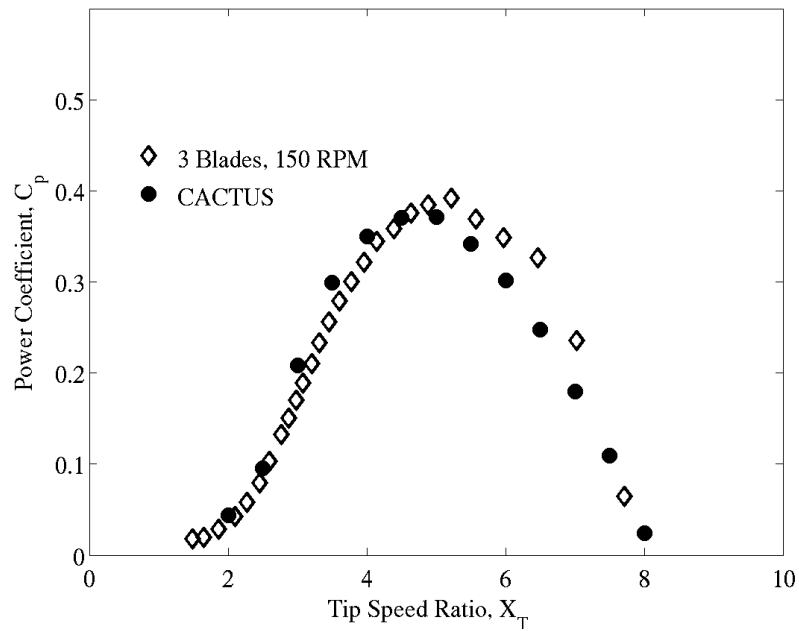


**Figure 10. Comparison of CACTUS power coefficient prediction with Sandia 5 meter VAWT measured data; 3 blades, 150 RPM.**



### E. Sandia 34m VAWT

The Sandia 34 meter diameter VAWT, shown in Figure 11, was conceived as a full scale test bed to investigate a structurally and aerodynamically optimized VAWT design. The turbine rotor consisted of two blades comprised of five segments, each with a different blade chord and airfoil section. The straight blade end segments connected to the tower have a 1.22 meter chord and make use of the NACA 0021 airfoil section. The equatorial section is a circular arc with a blade chord of 0.91 meters, using the Sandia 0018/50 laminar flow airfoil section. Circular arc transitions between the equatorial and end segments had a chord of 1.07 meters and also used the 0018/50 airfoil section. The rotor height to radius ratio was 2.46 and had a solidity of 0.13. No support struts were required.

Performance data for the Sandia 34 meter turbine were collected and averaged in order to obtain a mean performance curve, representing statistically averaged power coefficient versus mean wind speed at the rotor equator height. Datasets exist at 28, 34, and 38 RPM and are documented in Ref. (14). The data were cataloged with clean blades as well as with natural leading edge contamination. Clean blade data are used for this study.

An initial set of CACTUS simulations was performed for comparison with the Sandia 34 meter datasets, using a moderate discretization level. Each blade was discretized with a total of 13 lifting line elements, two elements on each straight end section, two elements on each transition section, and five elements on the equatorial section. Temporal advancement was performed with 30 time steps per revolution, and the simulation was carried out for 20 revolutions, or until the revolution average power coefficient converged to within 0.1%. Dynamic stall effects are represented with the modified Boeing-Vertol model. Excrescence drag was accounted for using the zero-wind speed torque data reported from the experiment. The measured zero-wind drag was nearly twice that predicted using only airfoil performance data in the relevant Reynolds number range. Performance data presented below consist of the revolution averages taken over the last revolution simulated.

Measured and predicted performance for the Sandia 34 meter VAWT is shown in Figure 12. Power coefficient and tip speed ratio are defined in Eqs. (24-25). The advance ratio used below is the inverse of the tip speed ratio. Generally good agreement is shown up to an advance ratio of 0.3. Beyond this point, the match degrades, indicating a potential deficiency in the dynamic stall modeling. CACTUS predicts a slight improvement in high tip speed ratio performance at 38 RPM due to decreased profile drag at higher Reynolds numbers. The data somewhat support this.



Figure 11. The Sandia 34 meter VAWT test bed.

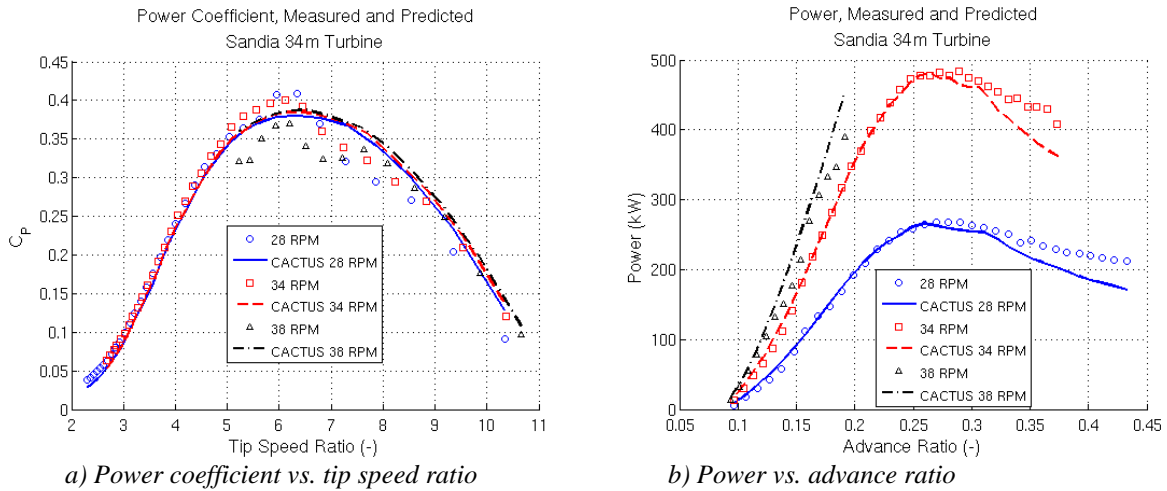
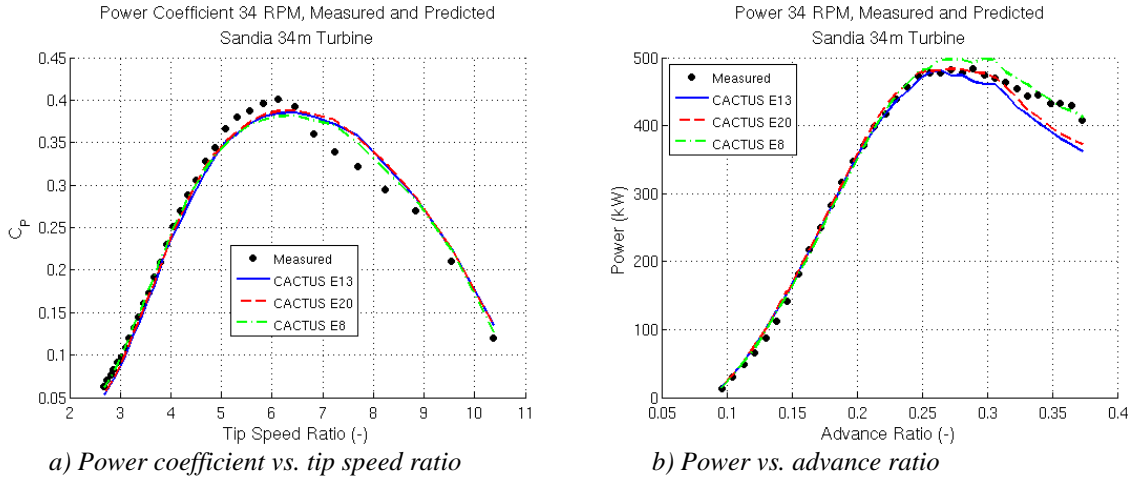


Figure 12. Measured and predicted performance data for the Sandia 34m VAWT, RPM variation.



The convergence of the CACTUS predicted revolution average performance data with varying blade element resolution was investigated using the 34 RPM dataset. The behavior of the prediction with increasing element resolution is illustrated in Figure 13, where *E8*, *E13*, and *E20* refer to the use of 8, 13, and 20 elements to resolve each blade. While none of these discretization levels show exceedingly poor performance, some amount of discrepancy is noted in the maximum predicted power using 8 elements per blade. The *E13* and *E20* discretizations produce revolution average performance predictions within 1% of one another, indicating a converged solution.



**Figure 13. Effect of blade element resolution on revolution average performance predictions.**

The convergence of the CACTUS predicted revolution average performance data with varying temporal resolution was investigated using the 34 RPM dataset. The effect of a wake velocity freezing technique on revolution average performance prediction is also investigated.

Freezing the wake velocity updates for a certain number of time steps has a significant effect on calculation time, as most of the computations performed by the simulation relate to updating the wake self-induced velocities. The number of time steps over which the wake velocities are left frozen is set equal to the tip speed ratio rounded down to the nearest integer, in order to leave the distance traveled by the wake nodes between velocity updates relatively constant.

The behavior of the prediction with increasing temporal resolution is illustrated in Figure 14, where *T20*, *T30*, and *T40* refer to the use of 20, 30, and 40 time steps to resolve each revolution of the turbine. The *i0* designation refers to the use of wake velocity freezing as described above. It can be noted that the use of wake velocity freezing on the *T20* discretization had little detrimental effect on the revolution average performance prediction. With the

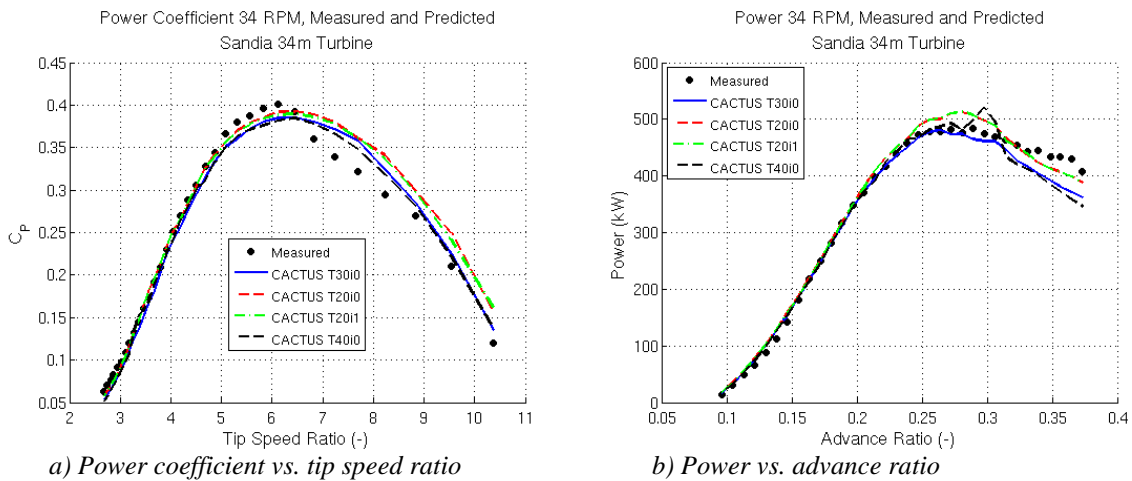


**Figure 14. Effect of temporal resolution on revolution average performance predictions.**

exception of the discrepancy in predicted power near an advance ratio of 0.3, the *T30* and *T40* discretizations produce revolution average performance predictions within 1% of one another, indicating a converged solution.

On inspection of the simulated individual element loads, the odd behavior of the *T40* discretization at an advance ratio near 0.3 can be related to non-physical effects resulting from a feedback loop between the wake induced flow velocities on the elements and the modified Boeing-Vertol dynamic stall model. This feedback mechanism appears to be most prevalent on the retreating blade side of the turbine, and at higher temporal resolution. This effect is most likely due to the algebraic nature of this dynamic stall model, with the hysteresis in stalled-flow blade element loads being instantaneously related to the angle of attack rate. Under stalled flow conditions, the angle of attack rate on each blade element is fairly sensitive to near-field wake induced velocities, and also has a strong effect on the strength of the near-field wake itself, through the blade element load. This system appears to become overly stiff at higher temporal resolution and this causes the observed non-physical effects. An initial investigation of this problem using the Leishman-Beddoes dynamic stall model showed no signs of these non-physical effects. This is most likely a result of the physical time constants placed on the simulated dynamic stall processes, which distinguish the Leishman-Beddoes model from the algebraic Boeing-Vertol approach.

## F. VAWT 850

The VAWT 850 demonstration machine was a straight-bladed VAWT that was tested at the UK Carmarthen Bay Wind Turbine Demonstration Centre in 1990<sup>15</sup>. The turbine rotor consisted of two blades, attached at mid-span to a crossarm member, which connected the blades to the top of a central tower containing the rotor bearing and drive train (see Figure 15). The blades were 24.3 m long, and tapered such that the tip chord was 75% of the mid-span chord. The mean chord of the blades was 1.75 m. The blade foils were NACA0018 sections, while the crossarm consisted of an outer section with NACA0030 cross-section and an inner section with an elliptical cross-section. For this study the crossarm is modeled as a constant chord member with NACA0030 section along its entire length and chord equal to the blade mid-span chord. Hub height for the machine was 30 m, and the diameter was 35 m. The rated power of the machine was 500 kW at a rotational speed of 20.4 RPM, although published performance data are apparently only available for a rotational speed of 13.62 RPM.

The published power curve gives generator power versus wind speed. In order to compare the data with numerical predictions, the generator is converted to a rotor power using an assumed drive train efficiency of 90%. This assumption and the associated uncertainty in experimental rotor power should be considered when comparing the data to the predictions. Another source of uncertainty is the interference drag due to the blade-strut attachment and its associated hardware (see photograph in Figure 15). The empirical relations described earlier were used to model the crossarm drag and the attachment interference drag. An additional excrescence drag with a drag coefficient of 0.2 based on the square of the blade chord at the attachment point was also added. The value of 0.2 was chosen so that good agreement between predictions and data was obtained at high tip-speed ratios. A better approach would be to estimate the excrescence drag from experimental characterization of the machine; however, in this case such data did not exist. This test case highlights the critical importance of characterizing blade-strut attachment drag for accurate prediction of cross-flow turbine performance.

CACTUS simulations of the VAWT 850 were performed at the 13.62 RPM operating condition for which data were available. The model incorporated 16 blade elements per blade, and 20 time steps per rotor revolution. A total of 15 revolutions were simulated for tip speed ratios of less than 4, and 25 revolutions were simulated for higher tip speeds. The modified Boeing-Vertol dynamic stall model was used in these simulations. Figure 16 compares the experimental data for rotor power and power coefficient to CACTUS predictions. Very good agreement is obtained for the  $C_p$  curve, although it should be stressed that the excrescence drag was chosen to ensure good agreement at high tip speed ratio. The stall wind speed and power level at stall is well-predicted, but the post-stall power is underpredicted at higher wind speeds. These results again indicate room for improvement in the dynamic stall model.

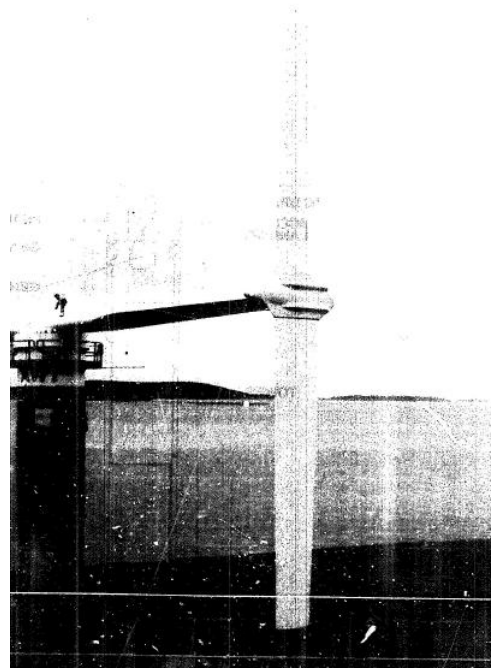
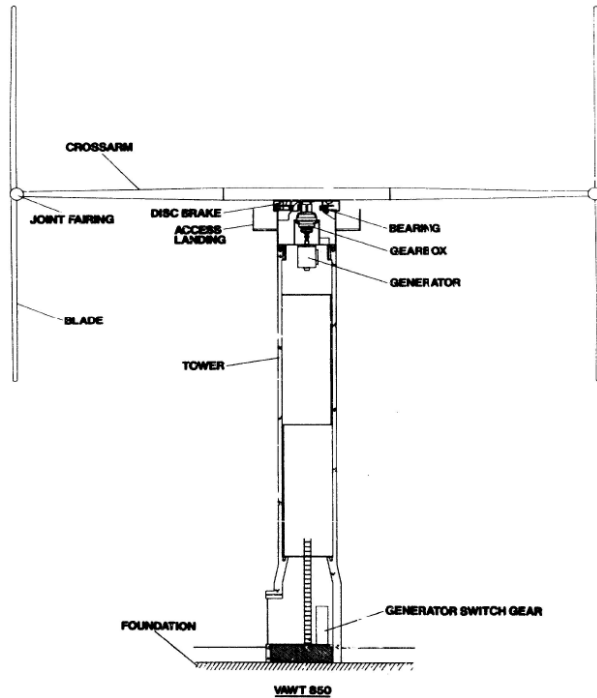
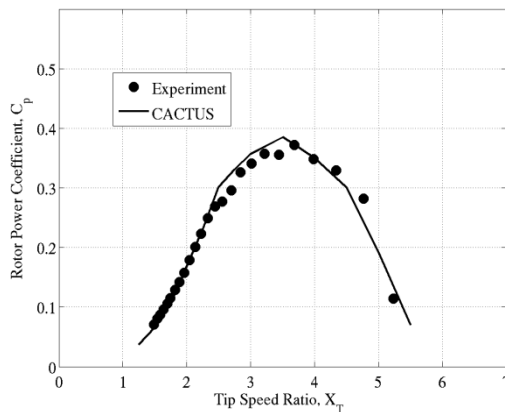
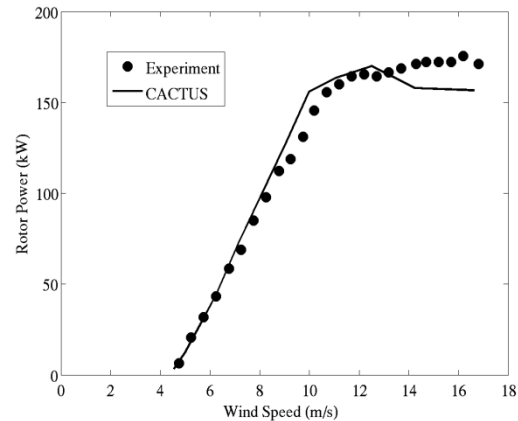


Figure 15. VAWT 850 schematic and photograph of the blade-crossarm attachment (Figures from Ref. (15)).



a) Power coefficient vs. tip speed ratio



b) Power vs. wind speed

Figure 16. Measured and predicted rotor performance for the VAWT 850, 13.62 RPM.

#### IV. Future Enhancements

##### A. Cavitation Onset Prediction

Cavitation in a hydrodynamic flow is a condition that occurs when the fluid pressure at some point in the flow decreases to a value close to the fluid vapor pressure. If this condition is reached, a vapor cavity can begin to form within the surrounding fluid, altering the flow characteristics. The formation and dynamics of the vapor cavity are unstable and violent. As such, cavitation is a condition to be avoided in normal turbine operation in order to avoid damage to the rotor. While predictions of turbine performance in cavitating flow conditions are beyond the scope of this model, the ability to predict the onset of cavitation on the rotor is desired. This can be accomplished by comparing the pressure at which cavitation onset is expected to the turbine simulation prediction of the minimum pressure achieved on all blade elements that comprise the rotor. Minimum pressure as a function of local blade section angle of attack may be input as part of the foil performance data.

## B. Wake Velocity Calculation Acceleration

The CACTUS code currently runs in seconds to minutes on a workstation, depending on the number of rotor revolutions simulated and the temporal resolution desired. For statistical load cases or for optimization studies, where many hundreds of simulations may be required, reduction in computational time would be useful. One option for achieving speedup would be to implement some or all of the calculation in parallel on a graphics processing unit (GPU). In recent years, NVIDIA has exposed the high-throughput arithmetic capability of their GPU devices such that the GPU itself can be used for scientific computing. Many have reported significant gains in performance with this architecture when compared to similarly parallelized calculations executed on CPU clusters. The NVIDIA CUDA language could provide a means for rapidly porting the existing wake system calculation to a parallel computation executed on a compatible NVIDIA device.

## C. Wake Advancement

CACTUS currently uses a second-order predictor explicit time advancement scheme to advance the wake node positions in time. The scheme is based on the midpoint rule, with the state derivatives (wake node velocities) predicted at time  $t + \frac{\Delta t}{2}$  using the wake node velocities for the existing and previous time steps. It would be generally beneficial to have the option of adding a corrector step to this method, although this would essentially double the computation time for a given temporal resolution. This would be particularly beneficial for simulations at high tip speed ratio, where non-linear interactions between the densely packed wake lines in the near wake are more important.

## D. Panel Element Blades

Due primarily to increased working fluid density as well as structural considerations, some proposed MHK turbine systems have rotor solidity values considerably larger than wind turbine systems of similar concept. For these rotor configurations, the local two-dimensional flow assumption on which the lifting line theory is founded may not be valid. As such, implementation of full geometry blade structures is a planned addition to CACTUS, using potential flow panel elements to represent an arbitrary blade shape. At present, the panel method under investigation describes bodies of arbitrary shape by a number of vortex ring panels, or facets, on the surface of the body. The Neumann, or zero normal flow, boundary condition is used on the surface of the blade. The vortex ring formulation allows for fairly seamless integration with the wake models already implemented for the lifting line blades.

## E. Shrouds and Nearby Structures

While CACTUS currently simulates only the rotor component of the turbine, in many MHK systems, other nearby structures may impact the performance and loads of the rotor. These may include diffuser shrouds, blade support struts, rotor hub and support towers, or floating barge platforms. Planned implementations of these types of geometry objects will leverage the work done on the panel element blade geometry implementation.

## Acknowledgments

This work was performed by Sandia National Laboratories supported by the United States Department of Energy's Wind and Water Power Program. Sandia is a multiprogram laboratory operated by Sandia Corporation, a Lockheed-Martin company, for the United States Department of Energy's National Nuclear Security Administration under Contract DE-AC04-94AL85000.

## References

- <sup>1</sup>Strickland, J. H., Smith, T., Sun, K., "A Vortex Model of the Darrieus Turbine: An Analytical and Experimental Study," Sandia National Laboratories, SAND81-7017, Albuquerque, NM, 1981.
- <sup>2</sup>Katz, J., and Plotkin, A., *Low Speed Aerodynamics*, 2<sup>nd</sup> ed., Cambridge University Press, Cambridge, England, UK, 2001, Chaps. 2, 6, 10, 12, 15.
- <sup>3</sup>Paraschivoiu, I., *Wind Turbine Design: With Emphasis on Darrieus Concept*, Polytechnic International Press, Montreal, CA, 2002.
- <sup>4</sup>Newman, J. N., *Marine Hydrodynamics*, MIT Press, Cambridge, MA 1977, Chap. 6.
- <sup>5</sup>Faltinsen, O. M., *Hydrodynamics of High-Speed Marine Vehicles*, Cambridge University Press, Cambridge, UK, 2005, Ch. 4.
- <sup>6</sup>Gormont, R. E., "A Mathematical Model of Unsteady Aerodynamics and Radial Flow for Application to Helicopter Rotors," U.S. Army Air Mobility R&D Lab., DAAJ02-71-C-0045, 1973.
- <sup>7</sup>Leishman, J. G., Beddoes, T. S., "A Semi-Empirical Method for Dynamic Stall," *Journal of the American Helicopter Society*, Vol. 34, 1989, pp. 3-17.

- <sup>8</sup>Leishman, J.G., Beddoes T.S., "A Generalised Model for Airfoil Unsteady Aerodynamic Behaviour and Dynamic Stall Using the Indicical Method," *Presented at the 42<sup>nd</sup> Annual Forum of the American Helicopter Society*, Washington D.C., June, 1986.
- <sup>9</sup>Gupta, S., Leishman, J.G. "Dynamic Stall Modeling of the S809 Airfoil and Comparison with Experiments," *Wind Energy*, Vol. 9, John Wiley & Sons, Ltd., 2006, pp. 521-547
- <sup>10</sup>Bjorck, A., "DYNSTALL: subroutine package with a dynamic stall model," The Aeronautical Research Institute of Sweden, Technical Report FFAP-V-110, 2000.
- <sup>11</sup>Galvanetto, U., Piero, J., Chantharasenawong, C., "An assessment of some effects of the nonsmoothness of the Leishman–Beddoes dynamic stall model on the nonlinear dynamics of a typical aerofoil section," *Journal of Fluids and Structures*, Vol. 24, 2008, pp. 151-163.
- <sup>12</sup>Sheldahl, R.E., Klimas, P.C., and Feltz, L.V. "Aerodynamic Performance of a 5-Metre-Diameter Darrieus Turbine with Extruded Aluminum NACA-0015 Blades," Sandia National Laboratories, SAND80-0179, Albuquerque, NM, March, 1980.
- <sup>13</sup>Sheldahl, R.E. and Klimas, P.C. "Aerodynamic Characteristics of Seven Symmetrical Airfoil Sections through 180-Degree Angle of Attack for Use in Aerodynamic Analysis of Vertical Axis Wind Turbines," Sandia National Laboratories, SAND80-2114, Albuquerque, NM, March, 1981.
- <sup>14</sup>Ashwill, T.D. "Measured Data for the Sandia 34-Meter Vertical Axis Wind Turbine," Sandia National Laboratories, SAND91-2228, Albuquerque, NM, July, 1992.
- <sup>15</sup>Mays, I.D., Morgan, C.A., Anderson, M.B., and Powles, S.J.R. "Experience with the VAWT 850 Demonstration Project," *European Community Wind Energy Conference*, September 1990.
- <sup>16</sup>Hoerner, S. F. *Fluid Dynamic Drag*. Second Edition, Published by Author, 1965.
- <sup>17</sup>Leishman, J. G., "Challenges in Modeling the Unsteady Aerodynamics of Wind Turbines," *Wind Energy*, Vol. 5, No. 2, John Wiley & Sons, Ltd., 2002, pp. 85-132
- <sup>18</sup>Leishman, J. G., Bhagwat, J. M., Bagai, A., "Free Vortex Filament Methods for the Analysis of Helicopter Rotor Wakes," *AIAA Journal of Aircraft*, Vol. 39, No. 5, 2002, pp. 759-775.
- <sup>19</sup>Gupta, S. and Leishman, J.G. "Comparison of momentum and vortex methods for the aerodynamic analysis of wind turbines," AIAA Paper 2005-594, 2005.
- <sup>20</sup>Cline, S. and Crawford, C. "Comparison of potential flow wake models for horizontal-axis wind turbine rotors," AIAA Paper 2010-463, 2010.
- <sup>21</sup>Dixon, K., Simao Ferreira, C., Hofemann, C., van Bussel, G., and van Kuik, G. "A 3D unsteady panel method for vertical axis wind turbines," In Chaviaropoulos, T., editor, *The Proceedings of the European Wind Energy Conference and Exhibition, EWEC 2008, Brussels*.
- <sup>22</sup>Peters, D.A., Boyd, D.D., He, C.J. "Finite-state induced-flow model for rotors in hover and forward flight," *J. American Helicopter Society*, 34(4):5-17, 1989.